We find that for both consumption and assets, models trained in-country uniformly outperform models trained out-of-country (Fig. 5), as would be expected. But we also find that models appear to "travel well" across borders, with out-of-country predictions often approaching the accuracy of in-country predictions. Pooled models trained on all four consumption surveys or all five asset surveys very nearly approach the predictive power of in-country models in almost all countries for both outcomes. These results indicate that, at least for our sample of countries, common determinants of livelihoods are revealed in imagery, and these commonalities can be leveraged to estimate consumption and asset outcomes with reasonable accuracy in countries where survey outcomes are unobserved.

Discussion

Our approach demonstrates that existing high-resolution daytime satellite imagery can be used to make fairly accurate predictions about the spatial distribution of economic well-being across five African countries. Our model performs well despite inexact data on both the timing of the daytime imagery and the location of clusters in the training data, and more precise data in either of these dimensions are likely to further improve model performance.

Notably, we show that our model's predictive power declines only modestly when a model trained in one of our sample countries is used to estimate consumption or assets in another country. Despite differences in economic and political institutions across countries, model-derived features appear to identify fundamental commonalities in the determinants of livelihoods across settings, suggesting that our approach could be used to fill in the large data gaps resulting from poor survey coverage in many African countries. In contrast to other recent approaches that rely on proprietary commercial data sets, our method uses only publicly available data and so is straightforward and nearly costless to scale across countries.

Although our model outperforms other sources of passively collected data (e.g., cellphone data, nightlights) in estimating economic well-being at the cluster level, we are currently unable to assess its ability to discern differences within clusters, as public-domain survey data assign identical coordinates to all households in a given cluster to preserve respondent privacy. In principle, our model can make predictions at any resolution for which daytime satellite imagery is available, though predictions on finer scales would likely be noisier. New sources of ground truth data, whether from more disaggregated surveys or novel crowdsourced channels, could enable evaluation of our model at the household level. Combining our extracted features with other passively collected data, in locations where such data are available, could also increase both household- and cluster-level predictive power.

Given the limited availability of high-resolution time series of daytime imagery, we also have not yet been able to evaluate the ability of our transfer learning approach to predict changes in economic well-being over time at particular locations. Such predictions would be very helpful to both researchers and policy-makers and should be enabled in the near future as increasing amounts of high-resolution satellite imagery become available (*22*).

Our transfer learning strategy of using a plentiful but noisy proxy shows how powerful machine learning tools, which typically thrive in data-rich settings, can be productively employed even when data on key outcomes of interest are scarce. Our approach could have broad application across many scientific domains and may be immediately useful for inexpensively producing granular data on other socioeconomic outcomes of interest to the international community, such as the large set of indicators proposed for the United Nations Sustainable Development Goals (*5*).

REFERENCES AND NOTES

1. United Nations, "A World That Counts: Mobilising the Data Revolution for Sustainable Development" (2014).
2. S. Devarajan, *Rev. Income Wealth* **59**, S9–S15 (2013).
3. M. Jerven, *Poor Numbers: How We Are Misled by African Development Statistics and What to Do About It* (Cornell Univ. Press, 2013).
4. World Bank, PovcalNet online poverty analysis tool, http://iresearch.worldbank.org/povcalnet/ (2015).
5. M. Jerven, "Benefits and costs of the data for development targets for the Post-2015 Development Agenda," Data for Development Assessment Paper Working Paper, September (Copenhagen Consensus Center, Copenhagen, 2014).
6. J. Sandefur, A. Glassman, *J. Dev. Stud.* **51**, 116–132 (2015).
7. J. V. Henderson, A. Storeygard, D. N. Weil, *Am. Econ. Rev.* **102**, 994–1028 (2012).
8. X. Chen, W. D. Nordhaus, *Proc. Natl. Acad. Sci. U.S.A.* **108**, 8589–8594 (2011).
9. S. Michalopoulos, E. Papaioannou, *Q. J. Econ.* **129**, 151–213 (2013).
10. M. Pinkovskiy, X. Sala-i-Martin, *Q. J. Econ.* **131**, 579–631 (2016).
11. J. Blumenstock, G. Cadamuro, R. On, *Science* **350**, 1073–1076 (2015).
12. L. Hong, E. Frias-Martinez, V. Frias-Martinez, "Topic models to infer socioeconomic maps," AAAI Conference on Artificial Intelligence (2016).
13. Y. LeCun, Y. Bengio, G. Hinton, *Nature* **521**, 436–444 (2015).
14. S. J. Pan, Q. Yang, *IEEE Trans. Knowl. Data Eng.* **22**, 1345–1359 (2010).
15. M. Xie, N. Jean, M. Burke, D. Lobell, S. Ermon, "Transfer learning from deep features for remote sensing and poverty mapping," AAAI Conference on Artificial Intelligence (2016).
16. D. Filmer, L. H. Pritchett, *Demography* **38**, 115–132 (2001).
17. D. E. Sahn, D. Stifel, *Rev. Income Wealth* **49**, 463–489 (2003).
18. O. Russakovsky *et al.*, *Int. J. Comput. Vis.* **115**, 211–252 (2014).
19. A. Krizhevsky, I. Sutskever, G. E. Hinton, *Adv. Neural Inf. Process. Syst.* **25**, 1097–1105 (2012).
20. National Geophysical Data Center, Version 4 DMSP-OLS Nighttime Lights Time Series (2010).
21. V. Mnih, G. E. Hinton, in *11th European Conference on Computer Vision, Heraklion, Crete, Greece, 5 to 11 September 2010* (Springer, 2010), pp. 210–223.
22. E. Hand, *Science* **348**, 172–177 (2015).

ACKNOWLEDGMENTS

We gratefully acknowledge support from NVIDIA Corporation through an NVIDIA Academic Hardware Grant, from Stanford's Global Development and Poverty Initiative, and from the AidData Project at the College of William & Mary. N.J. acknowledges support from the National Defense Science and Engineering Graduate Fellowship Program. S.E. is partially supported by NSF grant 1522054 through subcontract 72954-10597. We declare no conflicts of interest. All data and code needed to replicate these results are available at http://purl.stanford.edu/cz134jc5378.

SUPPLEMENTARY MATERIALS

www.sciencemag.org/content/353/6301/790/suppl/DC1
Materials and Methods
Figs. S1 to S22
Tables S1 to S3
References (*23*–*27*)

30 March 2016; accepted 6 July 2016
10.1126/science.aaf7894

STATISTICAL PHYSICS

Quantum thermalization through entanglement in an isolated many-body system

Adam M. Kaufman, M. Eric Tai, Alexander Lukin, Matthew Rispoli, Robert Schittko, Philipp M. Preiss, Markus Greiner*

Statistical mechanics relies on the maximization of entropy in a system at thermal equilibrium. However, an isolated quantum many-body system initialized in a pure state remains pure during Schrödinger evolution, and in this sense it has static, zero entropy. We experimentally studied the emergence of statistical mechanics in a quantum state and observed the fundamental role of quantum entanglement in facilitating this emergence. Microscopy of an evolving quantum system indicates that the full quantum state remains pure, whereas thermalization occurs on a local scale. We directly measured entanglement entropy, which assumes the role of the thermal entropy in thermalization. The entanglement creates local entropy that validates the use of statistical physics for local observables. Our measurements are consistent with the eigenstate thermalization hypothesis.

When an isolated quantum system is perturbed—for instance, owing to a sudden change in the Hamiltonian (a so-called quench)—the ensuing dynamics are determined by an eigenstate distribution that is induced by the quench (*1*). At any given time, the evolving quantum state will have amplitudes that depend on the eigenstates populated by the quench and the energy eigenvalues of the Hamiltonian. In many cases, however,

Department of Physics, Harvard University, Cambridge, MA 02138, USA.
***Corresponding author. Email: greiner@physics.harvard.edu**

such a system can be difficult to simulate, often because the resulting dynamics entail a large amount of entanglement (*2*–*5*). Yet, remarkably, this same isolated quantum system can thermalize under its own dynamics, unaided by a reservoir (Fig. 1) (*6*–*8*), so that the tools of statistical mechanics apply and challenging simulations are no longer required. In this case, most observables of a quantum state coherently evolving according to the Schrödinger equation can be predicted from a thermal ensemble and thermodynamic quantities. Even with infinitely many copies of this quantum state, these same observables are fundamentally unable to reveal whether this is a single quantum state or a thermal ensemble. In other words, a globally pure quantum state is apparently indistinguishable from a mixed, globally entropic thermal ensemble (*6*, *7*, *9*, *10*). Ostensibly, the coherent quantum amplitudes that define the quantum state in Hilbert space are no longer relevant, even though they evolve in time and determine the expectation values of observables. The dynamic convergence of the measurements of a pure quantum state with the predictions of a thermal ensemble, and the physical process by which this convergence occurs, are the experimental focus of this work.

Theoretical studies have, in many regards, clarified the role of quantum mechanics in statistical physics (*6*, *7*, *9*–*13*). The conundrum surrounding the agreement of pure states with extensively entropic thermal states is resolved by the counterintuitive effects of quantum entanglement. A canonical example of this point is the Bell state of two spatially separated spins: Although the full quantum state is pure, local measurements of just one of the spins reveals a statistical mixture with reduced purity. This local statistical mixture is distinct from a superposition because no operation on the single spin can remove these fluctuations or restore its quantum purity. In such a way, the spin's entanglement with another spin creates local entropy, which is called entanglement entropy. Entanglement entropy is not a phenomenon that is restricted to spins but exists in all quantum systems that exhibit entanglement. And although probing entanglement is a notoriously difficult experimental problem, this loss of local purity or, equivalently, the development of local entropy, establishes the presence of entanglement when it can be shown that the full quantum state is pure.

We directly observed a globally pure quantum state dynamically lose local purity to entanglement and, in parallel, become locally thermal. Recent experiments have demonstrated analogies between classical chaotic dynamics and the role of entanglement in few-qubit spin systems (*14*), as well as the dynamics of thermalization within an ion system (*15*). In addition, studies of bulk gases have shown the emergence of thermal ensembles and the effects of conserved quantities in isolated quantum systems through macroscopic observables and correlation functions (*16*–*19*). We are able to directly measure the global purity as thermalization occurs through single-particle resolved quantum many-body interference. In turn, we show that we can observe microscopically the role of entanglement in producing local entropy in a thermalizing system of itinerant particles, which is paradigmatic of the systems studied in statistical mechanics.

Below, we explore the equivalence between the entanglement entropy that we measured and the expected thermal entropy of an ensemble (*11*, *12*). We further address how this equivalence is linked to the eigenstate thermalization hypothesis (ETH), which provides an explanation for thermalization in closed quantum systems (*6*, *7*, *9*, *10*). The ETH is typically framed in terms of the small variation of observables (expectation values) associated with eigenstates that are close in energy (*6*, *7*, *10*), but the role of entanglement in these eigenstates is paramount (*12*). Fundamentally, the ETH implies an equivalence of the local reduced density matrix of a single excited energy eigenstate and the local reduced density matrix of a globally thermal state (*20*), an equivalence which is made possible only by entanglement and the impurity that it produces locally within a globally pure state. The equivalence ensures thermalization of most observable quantities after a quantum quench. Through parallel measurements of the entanglement entropy and local observables within a many-body Bose-Hubbard system, we were able to experimentally study this equivalence that lies at the heart of quantum thermalization.

Experimental protocol

For our experiments, we used a Bose-Einstein condensate of ^{87}Rb atoms loaded into a two-dimensional optical lattice positioned at the focus of a high-resolution imaging system (*21*, *22*). The system is described by the Bose-Hubbard Hamiltonian

$$\hat{H} = -(J_x \sum_{x,y} \hat{a}^{\dagger}_{x,y}\hat{a}_{x+1,y} + J_y \sum_{x,y} \hat{a}^{\dagger}_{x,y}\hat{a}_{x,y+1} + h.c.) + \frac{U}{2}\sum_{x,y} \hat{n}_{x,y}(\hat{n}_{x,y} - 1) \quad (1)$$

where $\hat{a}^{\dagger}_{x,y}$, $\hat{a}_{x,y}$, and $\hat{n}_{x,y} = \hat{a}^{\dagger}_{x,y}\hat{a}_{x,y}$ are the bosonic creation, annihilation, and number operators at the site located at $\{x,y\}$, respectively (*h.c.*, hermitian conjugate). Atoms can tunnel between neighboring lattice sites at a rate J_i (where i indicates the direction of tunneling) and experience a pairwise interaction energy U when multiple atoms occupy a site. We had independent control over the tunneling amplitudes J_x and J_y through the lattice depth, which could be tuned to yield from $J/U \ll 1$ to $J/U \gg 1$. In addition to the optical lattice, we were able to superimpose arbitrary potentials by using a digital micromirror device placed in the Fourier plane of our imaging system (*23*).

To initiate the experiment, we isolated a plaquette of 2 × 6 sites from a larger low-entropy Mott insulator with unity filling (Fig. 2A) (*24*), which produced two copies of a six-site Bose-Hubbard chain. At this point, each copy was in a product state of single-atom Fock states on each of the constituent sites. We then suddenly switched on tunneling in the x direction, whereas tunneling in the y direction was suppressed. Each chain was restricted to the original six sites by introducing a barrier at the ends of the chains to prevent tunneling out of the system. These combined steps quenched the six-site chains into a Hamiltonian for which the initial state represents a highly excited state that has substantial overlap with an appreciable number of energy eigenstates. Each chain represents an identical but independent copy of a quenched system of six particles on six sites, which evolves in the quenched Hamiltonian for a controllable duration.

We then measured the quantum purity or on-site number statistics (Fig. 2C). For the former, we appended to the quench evolution a beam splitter operation that interferes the two identical copies by freezing dynamics along the chain and allowing for tunneling in a projected double-well potential for a prescribed time (*25*). In the last step for both measurements, a potential barrier was raised between the two copies, and a one-dimensional time-of-flight in the direction transverse to the chain was performed to measure the resulting occupation on each site of each copy.

The ability to measure quantum purity is crucial to assessing the role of entanglement in our system. Tomography of the full quantum state would typically be required to extract the

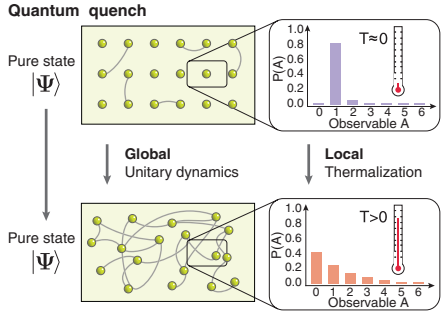

Fig. 1. Schematic of thermalization dynamics in closed systems. An isolated quantum system at zero temperature can be described by a single pure wavefunction $|\Psi\rangle$. Subsystems of the full quantum state are pure, as long as the entanglement between subsystems (indicated by the gray lines between the particles) vanishes (upper panels). If suddenly perturbed, the full system evolves unitarily, developing considerable entanglement between all parts of the system (lower panels). The bar graphs show the probability of an observable before and after perturbation of the system. Although the full system remains in a pure and in this sense zero-entropy state, the entropy of entanglement causes the subsystems to equilibrate, and local thermal mixed states appear to emerge within a globally pure quantum state.

global purity, which is particularly challenging in the full 462-dimensional Hilbert space defined by the itinerant particles in our system. Furthermore, whereas in spin systems global rotations can be used for tomography (*26*), there is no known analogous scheme for extracting the full density matrix of a many-body state of itinerant particles. The many-body interference described here, however, allows us to extract quantities that are quadratic in the density matrix, such as the purity (*25*). After performing the beam splitter operation, we were able to obtain the quantum purity of the full system and any subsystem simply by counting the number of atoms on each site of one of the six-site chains (Fig. 2C).

Each run of the experiment yielded the parity $P^{(k)} = \Pi_i p_i^{(k)}$, where i is iterated over a set of sites of interest in copy k. The single-site parity operator $p_i^{(k)}$ returns 1 (–1) when the atom number on site i is even (odd). It has been shown that the beam splitter operation yields $\langle P^{(1)} \rangle = \langle P^{(2)} \rangle = \mathrm{Tr}(\rho_1 \rho_2)$, where ρ_i is the density matrix on the set of sites considered for each copy (*4*, *25*, *27*). Because the preparation and quench dynamics for each copy are identical, yielding $\rho_1 = \rho_2 \equiv \rho$, the average parity reduces to the purity: $\langle P^{(k)} \rangle = \mathrm{Tr}(\rho^2)$. When the set of sites considered constitutes the full six-site chain, the expectation value of this quantity returns the global many-body purity, whereas for smaller sets it provides the local purity of the respective subsystem.

Comparing measurements taken with and without the beam splitter, our data immediately illustrate the contrast between the global and local behaviors and how thermalization is manifest (Fig. 2B). Our observations show that the global many-body state retains its quantum purity over time, affirming the unitarity of its evolution after the quench. This global measurement also clearly distinguishes the quantum state that we produced from a canonical thermal ensemble with a purity that is orders of magnitude smaller. Yet the number statistics locally converge to a distribution of thermal character, which can be faithfully modeled by that same thermal ensemble. We next experimentally explored the question suggested by this observation: How does a pure state that appears globally distinct from a thermal ensemble possess local properties that mirror this thermal state?

The growth of entanglement after a quench is key to understanding how entropy forms within the subsystems of a pure quantum state, thereby facilitating thermalization (*2*, *4*, *5*, *28*). When two parts of a system are entangled, the full quantum state ρ cannot be written in a separable fashion with respect to the Hilbert spaces of the subsystems (*29*, *30*). As has been shown theoretically (*4*, *27*) and recently observed experimentally (*25*), this causes the subsystems ρ_A and ρ_B to be in an entropic mixed state even though the full many-body quantum state is pure (*30*). The mixedness of the subsystem can be quantified by the second-order Rényi entropy $S_A = -\log[\mathrm{Tr}(\rho_A^2)]$, which is the natural logarithm of the purity of the subsystem density matrix. Although the von Neumann entropy is typically used in the context of statistical mechanics, both quantities grow as a subsystem density matrix becomes mixed and increasingly entropic. In the Rényi case, the purity in the logarithm quantifies the number of states contributing to the statistical mixture described by the density matrix.

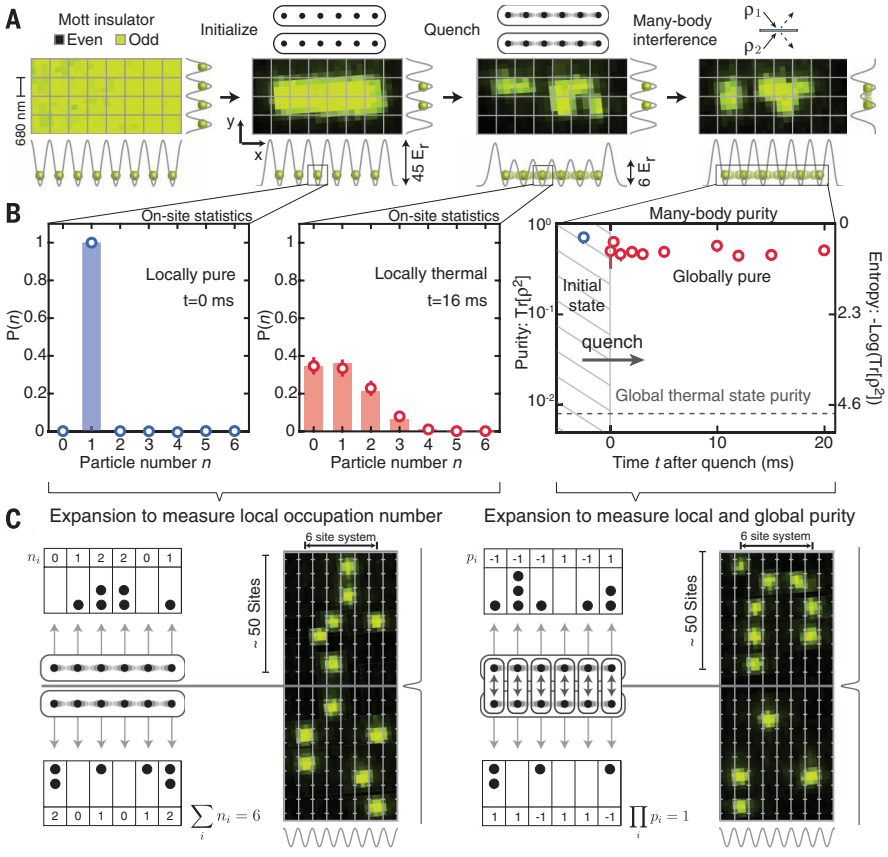

Fig. 2. Experimental sequence. (**A**) Using tailored optical potentials superimposed on an optical lattice, we deterministically prepared two copies of a six-site Bose-Hubbard system, where each lattice site is initialized with a single atom. We reduced the lattice depth along x (specified in units of the lattice recoil energy E_r) to enable tunneling and obtained either the ground state (adiabatic melt) or a highly excited state (sudden quench) in each six-site copy. After a variable evolution time, we froze the evolution and characterized the final quantum state by either acquiring number statistics or the local and global purity. Even and odd refer to the atom number parity. (**B**) Site-resolved number statistics of the initial distribution (left panel, showing a strong peak at one atom with vanishing fluctuations) and the distribution at later times (middle panel), compared with the predictions of a canonical thermal ensemble (red bars) of the same average energy as the quenched quantum state [$J/(2\pi)$ = 66 Hz; $U/(2\pi)$ = 103 Hz]. Error bars are SEM. Measurements of the global many-body purity show that it is static and high (right panel). This is in contrast to the vanishing global purity of the canonical thermal ensemble, yet this same ensemble accurately describes the local number distribution that we observed. (**C**) To measure the atom number locally, we allowed the atoms to expand in half-tubes along the y direction while pinning the atoms along x. In separate experiments, we applied a many-body beam splitter by allowing the atoms in each column to tunnel in a projected double-well potential. The resulting atom number parity (even or odd) on each site encodes the global and local purity.

Entanglement entropy dynamics and saturation

We first studied the dynamics of the entanglement entropy immediately after the quench for varying subsystem sizes (Fig. 3). Initially, we observed an approximately linear rise in the entropy with time, with a similar slope among the subsystems considered (Fig. 3, inset) (*2*). After an amount of time that depended on the subsystem size, the entanglement entropy saturated to a steady-state value, about which there were small residual temporal fluctuations. The presence of residual fluctuations is attributable in part to the finite size of our system. An exact numerical calculation of the dynamics with no free parameters shows excellent agreement with our experimental measurements. Crucially, the data indicate that whereas the subsystems acquire entropy with time (Fig. 3, A to C), the entropy of the full system remains constant and is small throughout the dynamics (Fig. 3D) (*24*). The high purity of the full

system allows us to conclude that the dynamical increase in entropy in the subsystems originates in the propagation of entanglement between the system's constituents. The approximately linear rise at early times (Fig. 3, inset) is related to the spreading of entanglement in the system within an effective light cone (*2*, *31*, *32*). Furthermore, in analogy to the growth of thermodynamic entropy in an equilibrating classical mechanical system, such as a gas in a closed container, we observed the growth of local entropy in a closed quantum mechanical system. In the quantum mechanical case, however, the mechanism responsible for the entropy is entanglement, which is absent from a system modeled by classical mechanics.

When a system thermalizes, we expect that the saturated values of local observables should correspond to the predictions of a statistical ensemble. By analogy, if the entanglement entropy plays the role of thermal entropy, then in a thermalized pure state, we expect extensive growth in the entanglement entropy with subsystem volume. When the entanglement entropy in a quantum state grows linearly with the size of the subsystem considered, it is known as a volume law. Theoretical work using conformal field theory has shown that indeed, at long times, a volume law is expected for a quenched, infinite, continuous system, whereas only an area law with a logarithmic correction is expected for the ground state (*2*, *33*, *34*). Characterizing the large amount of entanglement associated with a volume law is particularly challenging because it results in nearly every entry of the density matrix having a small but, importantly, nonzero magnitude.

Using the techniques outlined here, we obtained measurements showing a near-volume law in the entanglement entropy (Fig. 4A). A linear growth with volume in the entanglement entropy occurs when each subsystem incoherently populates a number of states that scales with the size of the subsystem Hilbert space. This is because, for the Bose-Hubbard model, the Hilbert space is approximately exponential in the lattice size, which results in a linear growth in $S_A = -\log[\mathrm{Tr}(\rho_A^2)]$. The exact slope of the entanglement entropy versus subsystem volume depends on the average energy of the thermalized pure state (*35*). In contrast, we can prepare the ground

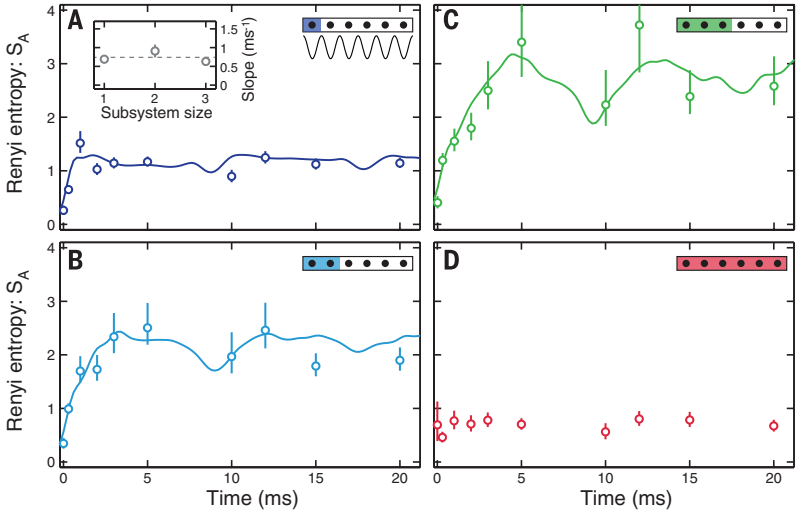

Fig. 3. Dynamics of entanglement entropy. Starting from a low-entanglement ground state, a global quantum quench leads to the development of large-scale entanglement between all subsystems. We quenched a six-site system from the Mott insulating product state ($J/U \ll 1$) with one atom per site to the weakly interacting regime of $J/U = 0.64$ [$J/(2\pi) = 66$ Hz] and measured the dynamics of the entanglement entropy. Shown are the dynamics for (**A**) one-, (**B**) two-, and (**C**) three-site subsystems and (**D**) the full system. As it equilibrates, a subsystem acquires local entropy, whereas the entropy of the full system remains constant and at a value given by measurement imperfections (D). The measured dynamics are consistent with exact numerical simulations (*24*) with no free parameters (solid lines). Error bars are SEM. For the largest entropies encountered in the three-site subsystem shown in (C), the large number of populated microstates leads to a significant statistical uncertainty in the entropy, which is reflected in the upper error bar extending to large entropies or being unbounded (*24*). The inset in (A) shows the slope of the early time dynamics, extracted from (A) to (C) with a piecewise linear fit (*24*). The dashed line is the mean of these measurements.

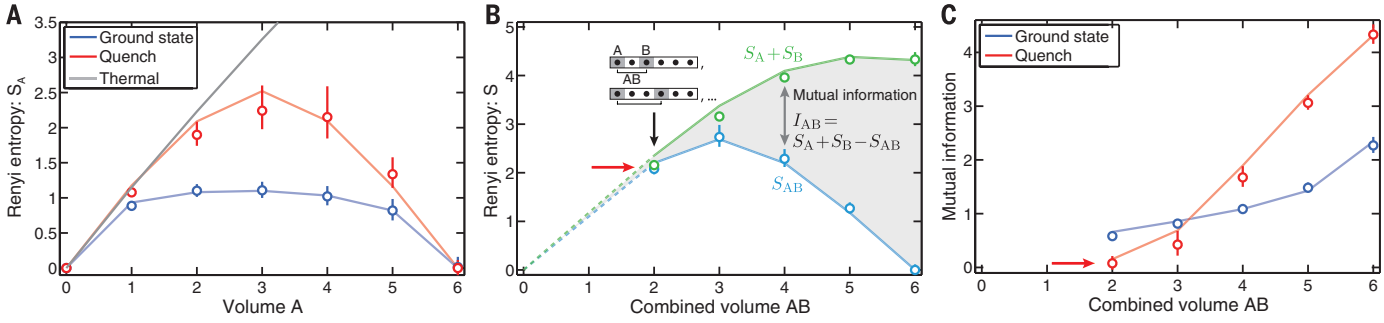

Fig. 4. Thermalized many-body systems. After the quench, the many-body state reaches a thermalized regime with saturated entanglement entropy. (**A**) In contrast to the ground state, for which the Rényi entropy only weakly depends on subsystem size, the entanglement entropy of the saturated quenched state grows almost linearly with size. As the subsystem size becomes comparable to the full system size, the subsystem entropy bends back to near zero, reflecting the globally pure zero-entropy state. For small subsystems, the Rényi entropy in the quenched state is nearly equal to the corresponding thermal entropy from the canonical thermal ensemble density matrix. (**B**) The mutual information $I_{AB} = S_A + S_B - S_{AB}$ quantifies the amount of classical (statistical) and quantum correlations between subsystems A and B (gray region). For small subsystems, the thermalized quantum state has $S_A + S_B \approx S_{AB}$, thanks to the near-volume law scaling (red arrow), leading to vanishing mutual information. When the volume of AB approaches the system size, the mutual information will grow because $S_A + S_B$ exceeds S_{AB}. (**C**) Mutual information I_{AB} versus the volume of AB for the ground state and the thermalized quenched state. For small system sizes, the quenched state exhibits smaller correlations than the adiabatically prepared ground state, and the mutual information is nearly vanishing (red arrow). When probed on a scale near the system size, the highly entangled quenched state exhibits much stronger correlations than the ground state. Throughout this figure, the entanglement entropies from the last time point in Fig. 3 are averaged over all relevant partitionings with the same subsystem volume; we have also corrected for the extensive entropy unrelated to entanglement (*24*). All solid lines represent numerical calculations with no free parameters (*24*).

state of the quenched Hamiltonian by adiabatically reducing the lattice depth. In this case, the superfluid ground state of the Bose-Hubbard model has suppressed entanglement, which is predicted to incur slow logarithmic growth in the entanglement entropy with subsystem volume (*33*). Our measurements clearly distinguish the two cases. The back-bending of the entanglement entropy as the subsystem surpasses half the system size indicates that the state is globally pure. In the quenched state, the high global purity is striking in a state that locally appears to be completely dephased, which is behavior often associated with environmentally induced decoherence or other noise sources.

We further observed near-quantitative agreement between the measured dependence of the entanglement entropy on subsystem volume and the prediction of a thermal ensemble. We made this comparison by computing a canonical thermal ensemble ρ^T (where T is temperature) with an average energy equal to that of the quenched quantum state that we produced experimentally (*35*). The gray line in Fig. 4A is the Rényi (thermal) entropy as a function of subsystem size for this calculated thermal state. Although our limited system size prevents comparison over a large range of subsystem sizes, the initial rise of the entanglement entropy with subsystem volume mimics that of the thermal entropy. Despite their similarity, it is worth emphasizing the disparate character of the thermal and entanglement entropies. The entanglement entropy (either Rényi or von Neumann) is instantaneously present in the pure quantum state after coherent unitary evolution, arising from the nonseparability of the quantum state between the subsystem and traced-out degrees of freedom. On the other hand, the von Neumann thermal entropy within a subsystem of a mixed thermal state is the thermodynamic entropy in statistical mechanics, which could be extracted from irreversible heat flow experiments on the subsystem (*12*). Therefore, the similarity of the Rényi entropies that we determined points to an experimental equivalence between the entanglement and thermodynamic entropies (*35*, *36*).

The behavior of the entanglement entropy provides a clean framework for understanding the entropy within thermalizing closed quantum systems. However, one of the most well-known features of entanglement, the presence of nonlocal correlations, appears inconsistent with what one expects of thermalized systems. In particular, the massive amount of entanglement implied by a volume law suggests high correlation between disparate parts of the system, whereas a key feature of a thermal state is the absence of such long-range correlations. A useful metric for correlations, both classical (statistical) and quantum, between two subsystems A and B is the mutual information $I_{AB} = S_A + S_B - S_{AB}$ (*25*, *37*). The mutual information demonstrates that the amount of correlation in the presence of a volume law is vanishing for subsystem volumes that sample less than half the full system, which is where the entropy growth is nearly linear (Fig. 4B). Furthermore, even though the thermalized quantum state carries more entanglement entropy than the ground state, small subsystems display smaller correlations in the thermalized quantum state than they do in the superfluid ground state (Fig. 4C). Once the subsystem volume is comparable to the system size, which is where the entanglement entropy deviates from the volume law, the quantum correlations entailed by the purity of the full system become apparent. The mutual information therefore illustrates how the volume law in the entanglement entropy yields an absence of correlations between sufficiently local observables, even though the quantum state retains a large amount of entanglement.

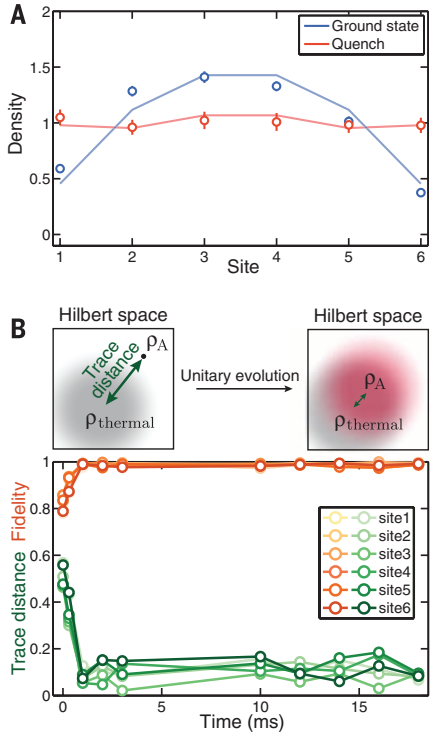

Fig. 5. Observation of local thermalization. (**A**) After quenching to J/U = 2.6, the saturated average particle number on each site (density) is nearly equal among the sites of the system, which resembles a system at thermal equilibrium. By comparison, the ground state for the same Bose-Hubbard parameters has appreciable curvature. (**B**) In measuring the probabilities of observing a given particle number on a single site, we can obtain the local single-site density matrix and observe the approach to thermalization. Using two different metrics—trace distance and fidelity—we compare the observed state to the mixed state derived from the subsystem of a canonical thermal ensemble after a quench to J/U = 0.64. The trace distance provides an effective distance between the mixed states in Hilbert space, whereas the fidelity is an overlap measure for mixed states. The two metrics illustrate how the pure state subsystem approaches the thermal ensemble subsystem shortly after the quench. The starting value of these quantities is given by the overlap of the initial pure state with the thermal mixed state. Solid lines connect the data points.

Local observables in the thermalized pure state

Our comparisons between the entanglement entropy and the thermal entropy suggest that the pure quantum state that we studied has thermalized properties. We further examined the presence of thermalization by performing a series of measurements of local observables with which we can compare the predictions of various thermal ensembles. As with the entanglement entropy, we can also contrast our observations of the quenched thermalized state with the adiabatically prepared ground state. In Fig. 5A, we show the in situ number density distribution on the six sites for the saturated quenched state and the (superfluid) ground state. Whereas the ground state exhibits considerable curvature, the quenched state exhibits a flat density distribution. This flat density distribution is consistent with a situation in which the constituents of the many-body system collectively thermalize, so that each site is in equilibrium with its neighbors and physically similar.

We can perform a more rigorous test of single-site thermalization by comparing the measured density matrix of each site with the reduced density matrix of a canonical thermal ensemble ρ_A^T (Fig. 5B). Our measurements of the probabilities of observing a given particle number on a site completely characterize that single-site density matrix because there are no coherences between different number states, thanks to superselection rules. With this measured density matrix, we can perform a quantitative comparison with a thermal ensemble by using the trace distance $\left(\frac{1}{2}\mathrm{Tr}(|\rho_A^T - \rho_A|)\right)$ and quantum fidelity $\left(\mathrm{Tr}\left(\sqrt{\sqrt{\rho_A^T}\rho_A\sqrt{\rho_A^T}}\right)\right)$, both of which quantify the similarity of two mixed quantum states. After a short time, these quantities show a quantum fidelity exceeding 99% and a trace distance that fluctuates between 0 and 0.1, indicating the similarity between the local density matrix of a verified pure state and the local density matrix of a thermal state. The correspondence between the observables of a pure state and a thermal state depends on the equivalence of their reduced density matrices within the Hilbert space sampled by the observable. The measurement in Fig. 5B therefore shows that observables for the single-site Hilbert space should agree with the predictions of thermal ensembles.

We now focus on direct comparisons of observables with various thermal ensembles and the theoretical justification for such comparisons. So far, we have focused on the role of entanglement entropy in producing thermal characteristics, but it is the eigenstate distribution resulting from a quench (Fig. 6A) that determines the dynamics of observables, as well as their subsequent saturated values. Therefore, these populated eigenstates should clarify the

origin of thermalization, which is the goal of the ETH. The underlying explanation for the ETH is that thermalizing, nonintegrable systems have excited eigenstates that look like nearly random vectors or, equivalently, are described by a Hamiltonian that approximately conforms to random matrix theory (*6*, *13*)—that is, for most bases, each eigenvector projects onto each basis vector with random quantum amplitude. The diffuse probability distribution of the eigenstates in most bases, such as the Fock state basis, is analogous to the chaotic dynamics of a closed classical mechanical system passing through every allowed point of phase space, and in the quantum case this has several consequences. Remarkably, this chaotic eigenstate assumption can be adapted to explain the saturation of measurement observables, the agreement of these saturated observables with thermal ensembles, and the presence of a volume law in the entanglement entropy (*6*, *13*, *38*, *39*). So, whereas in classical mechanical systems, it is the chaos in the temporal dynamics that leads to entropy maximization and thermalization within thermodynamic constraints, in quantum thermalizing systems, it is chaos in the energy eigenstates that generates the analogous behavior in the entanglement entropy and, in turn, causes thermalization.

In Fig. 6, C and D, we compare our measurements to the predictions of thermal ensembles that are illustrated in Fig. 6B. We also compare our results to a grand-canonical ensemble truncated to our total atom number (*24*); this ensemble perhaps most closely models how well the many-body state can act as a reservoir for its constituent subsystems. For each single-site and three-site observable, we show the atom number distributions for two different effective temperatures of 3.8J and 11J, which are achieved by quenching to J/U = 0.64 and J/U = 2.6, respectively. The data are averaged in the saturated regime over times between 10 and 20 ms, and the error bars are the standard deviation in the measured probabilities. The agreement within the error bars indicates that in this temporal range, our observations remain near the thermal predictions, despite the presence of temporal fluctuations. For the single-site subsystem, the data are in good agreement with all the ensembles considered. Despite the fact that the quenched state is in a large distribution of eigenstates, our data show agreement for the case of a single eigenstate ensemble; this illustrates a key principle of the ETH, which holds that the reduced density matrix and associated observables vary slowly from eigenstate to eigenstate and are therefore relatively insensitive to the breadth of the distribution of populated states from the quench. We show the same comparisons for the three-site case in the bottom two panels. In this case, there is also agreement with most ensembles, though there is relatively less agreement with the single eigenstate and grand-canonical ensembles, particularly for the lower-temperature quench. This variation in agreement may indicate that these ensembles are more sensitive to how the size of the traced-out reservoir compares with the size of the subsystem, which suggests directions for further experiments (*11*, *40*).

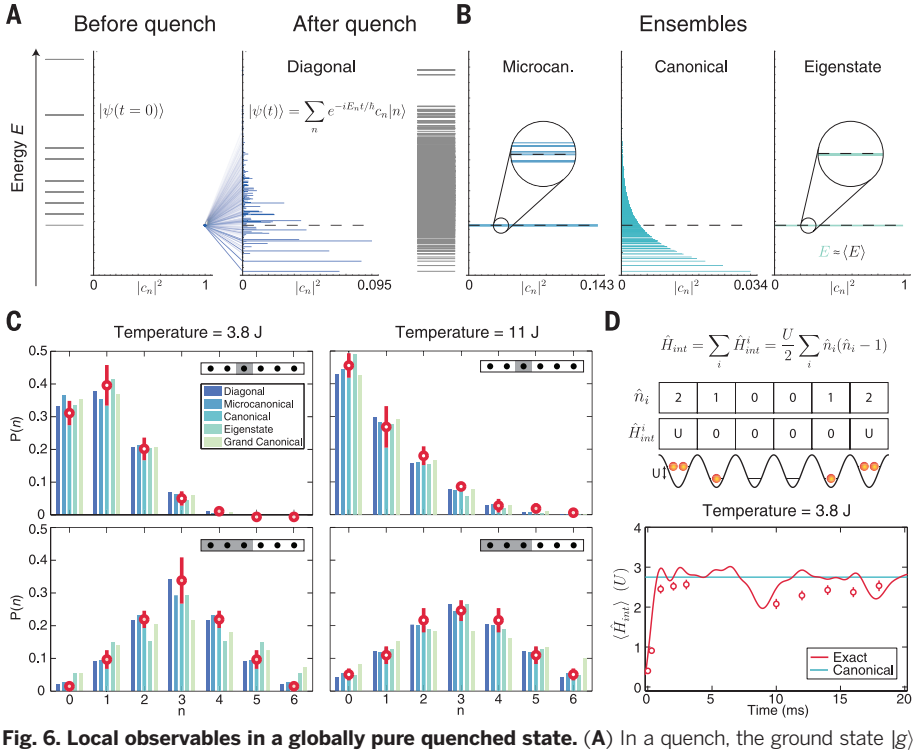

Fig. 6. Local observables in a globally pure quenched state. (**A**) In a quench, the ground state $|g\rangle$ of the initial Hamiltonian (represented in its eigenbasis in the first panel) is projected onto many eigenstates $|n\rangle$ of the new Hamiltonian. The full quantum state undergoes unitary evolution according to the eigenstate amplitudes and energies, c_n and E_n, respectively. $\langle E \rangle$ denotes the full system energy expectation value; $\hbar$ is the reduced Planck's constant. According to the ETH, the expectation value of observables at long times can be obtained from a diagonal ensemble (illustrated by the probability weights in the eigenstates of the quenched Hamiltonian), as well as from a microcanonical ensemble. (**B**) Along with the microcanonical ensemble, several other closely related ensembles (colored lines) are compared to the data. The dashed line indicates the expectation value of the full system energy. (**C**) Thermalization of local observables. For the different temperatures and subsystems shown, the measured number statistics are in excellent agreement with microcanonical and canonical thermal ensembles, verifying the thermal character of the local density matrix (*24*). A grand-canonical ensemble reproduces the data very well, as long as the subsystem is small compared with the full system. The error bars are the standard deviation of our observations over times between 10 and 20 ms. (**D**) Thermalization occurs even for global quantities such as the full-system interaction energy $\langle \hat{H}_{int} \rangle$. The thermalization dynamics as calculated from our number-resolved images are in close agreement with exact numerical simulation and a canonical prediction (*24*). Error bars are SEM.

The above measurements were performed on specific subsystems, but this technique allows extraction of the average global interaction energy (Fig. 6D). Because the interaction term in Eq. 1 is diagonal in the Fock state basis, we can use our measurements of the final particle configurations to compute the expectation value $\langle \hat{H}_{int} \rangle$. For the T = 3.8J data, we show a time series of the initial growth in this quantity, which starts at zero because the initial state has a single particle per site. At long times, these observations are in near agreement with the canonical prediction. This measurement is sensitive to the entire six-site system as opposed to some subset of sites, which might suggest that it is global and unlikely to thermalize. Yet $\langle \hat{H}_{int} \rangle$ undergoes thermalization because it is a sum of local operators, each of which thermalizes and is insensitive to the global purity of the full system. The observed agreement is consistent with the idea that only a small set of operators, such as the global purity that we measured or other specific fine-tuned state projectors, can truly distinguish the pure state that we produced from a thermal state.

Discussion

Our observations speak to a natural mapping between thermalizing quantum mechanical systems and classical mechanical systems composed of itinerant particles. Classical statistical mechanics relies on a fundamental assumption: A system in thermal equilibrium can be found in any microstate that is compatible with the thermodynamic constraints imposed on the system and, as such, is described by an ensemble of maximal entropy (*41*, *42*). Although it is vastly successful, classical statistical mechanics does not itself justify this entropy maximization for closed systems (*13*, *41*), and an open-systems approach only defers the

question of thermalization to the union of the bath and the system (*6*). Although ergodicity and time-averaging can provide a justification for entropy maximization in closed classical mechanical systems, ergodicity is not applicable on the same scale at which statistical mechanics is successful, and time-averaging can require exponentially long times (*13*, *41*, *42*). The latter also obscures the fact that there is in reality only one system, which, nevertheless, is well modeled by an entropic ensemble (*41*). Our study, as well as recent theoretical work (*11*, *12*, *35*), hint at a microscopic origin for entropy maximization in a single quantum state, namely, that which is induced by the entanglement that we have measured. Quantum mechanics does not require time-averaging; a single quantum state yields thermalized local observables, and these observables cannot distinguish this thermalized pure state from a mixed thermal ensemble of the same thermodynamic character.

Our measurements open up several avenues for further investigation. Instead of operating with a fixed total system size, it is possible to study how thermalization and fluctuations depend on the size of the system considered (*40*). Conversely, studying integrable Hamiltonians where thermalization fails (*43*), as well as the structure of the associated eigenstate spectrum of such systems, could allow direct tests of the relationship between conserved quantities and thermalization of a quantum state. Lastly, the application of these tools for characterizing the presence of thermalization and entanglement entropy could be powerful in studies of many-body localization, where one of the key experimental signatures is the logarithmic growth of entanglement entropy at long times and the suppression of precisely the thermalization that we have measured in this work (*20*, *44*–*47*).

REFERENCES AND NOTES

1. J. J. Sakurai, *Modern Quantum Mechanics* (Addison Wesley Longman, 1993).
2. P. Calabrese, J. Cardy, *J. Stat. Mech.* **2005**, P04010 (2005).
3. L. Amico, R. Fazio, A. Osterloh, V. Vedral, *Rev. Mod. Phys.* **80**, 517–576 (2008).
4. A. J. Daley, H. Pichler, J. Schachenmayer, P. Zoller, *Phys. Rev. Lett.* **109**, 020505 (2012).
5. J. Schachenmayer, B. P. Lanyon, C. F. Roos, A. J. Daley, *Phys. Rev. X* **3**, 031015 (2013).
6. J. M. Deutsch, *Phys. Rev. A* **43**, 2046–2049 (1991).
7. M. Rigol, V. Dunjko, M. Olshanii, *Nature* **452**, 854–858 (2008).
8. J. Eisert, M. Friesdorf, C. Gogolin, *Nat. Phys.* **11**, 124–130 (2015).
9. R. V. Jensen, R. Shankar, *Phys. Rev. Lett.* **54**, 1879–1882 (1985).
10. M. Srednicki, *Phys. Rev. E* **50**, 888–901 (1994).
11. L. F. Santos, A. Polkovnikov, M. Rigol, *Phys. Rev. E* **86**, 010102 (2012).
12. J. M. Deutsch, H. Li, A. Sharma, *Phys. Rev. E* **87**, 042135 (2013).
13. L. D'Alessio, Y. Kafri, A. Polkovnikov, M. Rigol, https://arxiv.org/abs/1509.06411v1 (2015).
14. C. Neill *et al.*, https://arxiv.org/abs/1601.00600 (2016).
15. G. Clos, D. Porras, U. Warring, T. Schaetz, http://arxiv.org/abs/1509.07712 (2015).
16. S. Trotzky *et al.*, *Nat. Phys.* **8**, 325–330 (2012).
17. T. Langen, R. Geiger, M. Kuhnert, B. Rauer, J. Schmiedmayer, *Nat. Phys.* **9**, 640–643 (2013).
18. R. Geiger, T. Langen, I. E. Mazets, J. Schmiedmayer, *New J. Phys.* **16**, 053034 (2014).
19. T. Langen *et al.*, *Science* **348**, 207–211 (2015).
20. R. Nandkishore, D. A. Huse, *Annu. Rev. Condens. Matter Phys.* **6**, 15–38 (2015).
21. W. S. Bakr *et al.*, *Science* **329**, 547–550 (2010).
22. J. F. Sherson *et al.*, *Nature* **467**, 68–72 (2010).
23. P. Zupancic *et al.*, *Opt. Express* **24**, 13881–13893 (2016).
24. Materials and methods are available as supplementary materials on *Science* Online.
25. R. Islam *et al.*, *Nature* **528**, 77–83 (2015).
26. C. A. Sackett *et al.*, *Nature* **404**, 256–259 (2000).
27. R. N. Palmer, C. Moura Alves, D. Jaksch, *Phys. Rev. A* **72**, 042335 (2005).
28. K. R. A. Hazzard *et al.*, *Phys. Rev. A* **90**, 063622 (2014).
29. R. Horodecki, P. Horodecki, M. Horodecki, K. Horodecki, *Rev. Mod. Phys.* **81**, 865–942 (2009).
30. R. Horodecki, M. Horodecki, *Phys. Rev. A* **54**, 1838–1843 (1996).
31. M. Cheneau *et al.*, *Nature* **481**, 484–487 (2012).
32. P. Richerme *et al.*, *Nature* **511**, 198–201 (2014).
33. P. Calabrese, J. Cardy, *J. Stat. Mech.* **2004**, P06002 (2004).
34. J. Eisert, M. Cramer, M. B. Plenio, *Rev. Mod. Phys.* **82**, 277–306 (2010).
35. J. R. Garrison, T. Grover, https://arxiv.org/abs/1503.00729 (2015).
36. T. Grover, M. P. A. Fisher, *Phys. Rev. A* **92**, 042308 (2015).
37. M. M. Wolf, F. Verstraete, M. B. Hastings, J. I. Cirac, *Phys. Rev. Lett.* **100**, 070502 (2008).
38. D. N. Page, *Phys. Rev. Lett.* **71**, 1291–1294 (1993).
39. K. Hyungwon, "Quantum nonequilibrium dynamics: Transport, entanglement, and thermalization," thesis, Princeton University (2014).
40. V. Yurovsky, A. Ben-Reuven, M. Olshanii, *J. Phys. Chem. B* **115**, 5340–5346 (2011).
41. S. K. Ma, *Statistical Mechanics* (World Scientific, 1985).
42. K. Huang, *Statistical Mechanics* (John Wiley and Sons, 1963).
43. T. Kinoshita, T. Wenger, D. S. Weiss, *Nature* **440**, 900–903 (2006).
44. M. Žnidarič, T. Prosen, P. Prelovšek, *Phys. Rev. B* **77**, 064426 (2008).
45. J. H. Bardarson, F. Pollmann, J. E. Moore, *Phys. Rev. Lett.* **109**, 017202 (2012).
46. M. Serbyn, Z. Papić, D. A. Abanin, *Phys. Rev. Lett.* **110**, 260601 (2013).
47. M. Schreiber *et al.*, *Science* **349**, 842–845 (2015).

ACKNOWLEDGMENTS

We acknowledge helpful discussions with S. Choi, S. Dickerson, J. Eisert, M. Foss-Feig, D. Greif, M. Headrick, D. Huse, M. Olshanii, C. Regal, J. Schachenmayer, and M. Wall. We are supported by grants from the NSF, including an NSF Graduate Research Fellowship (to M.R.); the Gordon and Betty Moore Foundation's Emergent Phenomena in Quantum Systems initiative (grant GBMF3795); and the Multidisciplinary University Research Initiative programs of the Air Force Office of Scientific Research and the Army Research Office.

SUPPLEMENTARY MATERIALS

www.sciencemag.org/content/353/6301/794/suppl/DC1
Materials and Methods
Figs. S1 to S3
Tables S1 and S2

11 March 2016; accepted 11 July 2016
10.1126/science.aaf6725

REPORTS

GEOMORPHOLOGY

Northward migration of the eastern Himalayan syntaxis revealed by OSL thermochronometry

Georgina E. King,[1,2]* Frédéric Herman,[1] Benny Guralnik[3]

Erosion influences the dynamical evolution of mountains. However, evidence for the impact of surface processes on tectonics mostly relies on the circumstantial coincidence of rugged topography, high stream power, erosion, and rock uplift. Using the optically stimulated luminescence (OSL) thermochronometry technique, we quantified the spatial and temporal exhumation of the eastern Himalayan syntaxis. We found increasing exhumation rates within the past million years at the northeast end of the Namche Barwa–Gyala Peri dome. These observations imply headward propagation of erosion in the Parlung River, suggesting that the locus of high exhumation has migrated northward. Although surface processes influence exhumation rates, they do not necessarily engage in a feedback that sets the location of tectonic deformation.

The topography of mountain ranges results from the interplay between climate, tectonics, and surface processes (*1*). A key aspect of this interplay is considered to be that surface processes may influence the dynamics of actively deforming mountain ranges through a system of positive feedbacks involving tectonics and erosion [reviewed in (*2*)]. The efficacy of such a system has been emphasized in analog and numerical experiments (*3*–*5*), which predict that erosion, rather than tectonics, can control the locus of deformation and exhumation of rocks toward Earth's surface (*6*). However, field evidence that supports such models is mostly circumstantial (*5*–*13*) and is based on the observation of a spatial coincidence between rugged topography, high rates of rock uplift, high precipitation, high stream

[1]Institute of Earth Surface Dynamics, University of Lausanne, CH-1015 Lausanne, Switzerland. [2]Institute of Geography, University of Cologne, 50923 Cologne, Germany. [3]Netherlands Centre for Luminescence Dating and Soil Geography and Landscape group, Wageningen University, Post Office Box 47, 6700 AA Wageningen, Netherlands.
*Corresponding author. Email: georgina.king@gmail.com

Science

Quantum thermalization through entanglement in an isolated many-body system

Adam M. Kaufman, M. Eric Tai, Alexander Lukin, Matthew Rispoli, Robert Schittko, Philipp M. Preiss and Markus Greiner

Science **353** (6301), 794-800.
DOI: 10.1126/science.aaf6725

To thermalize, or not to thermalize?

Intuition tells us that an isolated physical system subjected to a sudden change (i.e., quenching) will evolve in a way that maximizes its entropy. If the system is in a pure, zero-entropy quantum state, it is expected to remain so even after quenching. How do we then reconcile statistical mechanics with quantum laws? To address this question, Kaufman *et al.* used their quantum microscope to study strings of six rubidium atoms confined in the wells of an optical lattice (see the Perspective by Polkovnikov and Sels). When tunneling along the strings was suddenly switched on, the strings as a whole remained in a pure state, but smaller subsets of two or three atoms conformed to a thermal distribution. The force driving the thermalization was quantum entanglement.

Science, this issue p. 794; see also p. 752